The Astrophysical Journal, 785:86 (11pp), 2014 April 20 doi:10.1088/0004-637X/785/2/86

FORWARD MODELING OF GYROSYNCHROTRON INTENSITY PERTURBATIONS BY SAUSAGE MODES

V. E. Reznikova[1,2], P. Antolin[3], and T. Van Doorsselaere[1]
[1] Centre for Mathematical Plasma Astrophysics, Department of Mathematics, KU Leuven, Celestijnenlaan 200B box 2400, B-3001 Leuven, Belgium; Veronika.Reznikova@wis.kuleuven.be
[2] Radiophysical Research Institute (NIRFI), Nizhny Novgorod 603950, Russia
[3] National Astronomical Observatory of Japan, 2-21-1 Osawa, Mitaka, Tokyo 181-8588, Japan
Received 2013 December 2; accepted 2014 March 1; published 2014 March 28

ABSTRACT

To determine the observable radio signatures of the fast sausage standing wave, we examine gyrosynchrotron (GS) emission modulation using a linear three-dimensional magnetohydrodynamic model of a plasma cylinder. Effects of the line-of-sight angle and instrumental resolution on perturbations of the GS intensity are analyzed for two models: a base model with strong Razin suppression and a low-density model in which the Razin effect was unimportant. Our finding contradicts previous predictions made with simpler models: an in-phase variation of intensity between low ($f < f_{\rm peak}$) and high ($f > f_{\rm peak}$) frequencies is found for the low-density model and an anti-phase variation for the base model in the case of a viewing angle of 45°. The spatially inhomogeneous character of the oscillating emission source and the spatial resolution of the model are found to have a significant effect on the resulting intensity.

Key words: Sun: flares – Sun: oscillations – Sun: radio radiation – waves

Online-only material: color figures

1. INTRODUCTION

The presence of quasi-periodic pulsations (QPPs) in light curves is quite a common, if not intrinsic, phenomenon of flare radio emission from single flaring loops (Kupriyanova et al. 2010). However, their origin still remains largely unknown. Such QPPs can be interpreted in terms of magnetohydrodynamic (MHD) oscillations (magnetoacoustic or Alfvén) of flaring loops, modulating the gyrosynchrotron (GS) emission of trapped nonthermal electrons (Rosenberg 1970). The other possible interpretations are periodic particle acceleration in current sheets (Aschwanden 1987) or in a current-carrying loop considered as an LCR-circuit (Zaitsev 1998). For a recent review on QPPs in solar flares and their possible excitation mechanisms see Nakariakov & Melnikov (2009).

Modeling of MHD oscillations can be very useful for coronal seismology, which uses waves and oscillations as a tool to examine the physical parameters of the solar corona by comparing observed wave properties with the oscillation models (for a review, see Nakariakov & Verwichte 2005). Recently coronal seismology has been used to constrain the density contrast, the plasma-β, and the mode number in a flaring region (Van Doorsselaere et al. 2011). The superior time cadence of radio telescopes gives an advantage in the study of short-period oscillations, such as the sausage mode, whose characteristic period is in the range of several to tens of seconds. However, due to limited spatial resolution, the seismology of flaring QPPs has been difficult. In recent years, upgrades of the existing instruments and the construction of new telescopes have led to a significant improvement in spatial resolution of solar radio observations. The new Atacama Large Millimeter/submillimeter Array (ALMA) telescope has started to operate and offers unprecedentedly high spatial resolutions from 0.″06 at 85 GHz to 0.″005 at 950 GHz. The Chinese Spectral Radio Heliograph (CSRH), which is on the final stage of the construction now, will observe the Sun at 0.4–15 GHz with time cadence 200 ms and spatial resolution up to 1.″4 at 15 GHz. The paper provides models required to interpret future solar observations with ALMA and CSRH.

The fast magnetoacoustic sausage mode is a periodic transverse contraction and expansion of the flux tube, mainly driven by the magnetic pressure. The term "sausage" refers to an axisymmetric motion with the azimuthal wavenumber $m = 0$ described in (Zaitsev & Stepanov 1975) and Edwin & Roberts (1983). It modulates the cross-sectional area of the flux tube, magnetic field, density, and temperature of the plasma. Moreover, variation of a tube radius will cause small changes of the angle between the line of sight (LOS) and the vector of the magnetic field. Variations of these quantities in the microwave source affect flaring emission. This mode can be generated by a shock wave (McLean et al. 1971), or an increase in gas pressure due to impulsive energy release (Zaitsev & Stepanov 1982).

The period of the sausage mode in the corona is mostly determined by the length of the hosting loop and the external Alfvén speed, thus leading to short periods (Nakariakov et al. 2003; Vasheghani Farahani et al. 2014). The first confident interpretation of a microwave intensity oscillation in terms of the sausage mode was based on observations utilizing the Nobeyama Radioheliograph (NoRH; Nakajima et al. 1994) at 17 and 34 GHz (Melnikov et al. 2005). This interpretation was based on the interrelation between the period (15 s) and the loop length, on microwave diagnostics, as well as the phase relation between pulsations in the loop leg and loop top.

Later possible detections of the sausage mode in radio observations have been reported again with the NoRH (Inglis et al. 2008), with the LYRA radiometer on board PROBA2 (Van Doorsselaere et al. 2011), and with the Owens Valley Solar Array (Mossessian & Fleishman 2012). The modulation characteristics of sausage modes in the hard X-ray range have been found by Zimovets & Struminsky (2010) with the *RHESSI* spectrometer (Lin et al. 2002).

A number of studies on modeling the microwave emission pulsations produced by the sausage loop oscillations in solar flares were made in an attempt to find observable radio signatures of this mode. Kopylova et al. (2002) analytically analyzed the effect and found that in the case of the nonthermal GS

mechanism, the fluxes from optically thin and optically thick sources should be modulated in anti-phase. Later, Reznikova et al. (2007) showed that coherent behavior of the GS intensity variation at frequencies higher and lower than the peak frequency is expected in the case of high plasma density, when the low-frequency turnover of the microwave spectrum is due to the Razin effect. If GS radiation is suppressed at frequencies where the refractive index becomes significantly less than unity, it is often called the Razin effect (Razin 1960a, 1960b).

Mossessian & Fleishman (2012) confirmed that in the case of absence of the Razin suppression the oscillation phase changes by π around the peak frequency. They also showed that the modulation amplitude displays a curve with a minimum around the frequency of the spectral peak. The modulation in the optically thin regime exceeds a few times the modulation in the optically thick regime.

We would like to stress that none of mentioned models included spatial dependence; only the time dependence of the mode was treated. The main reason for that was the long time required to compute the exact GS emissivity and absorption coefficient, for which multiple calculations are needed to build a realistic three-dimensional (3D) model. The requirements of numerical integration of the radiation transfer equation along many LOSs of nonuniform sources complicated the entire treatment. However, the increasing resolution of solar radio observations calls for the corresponding 3D modeling of radio emission. Only with a 3D model can one correctly investigate the effects of LOS angle and instrumental resolution on perturbations of the radio emission. Fleishman & Kuznetsov (2010) recently developed approximate GS codes capable of fast calculation of the GS emission throughout a broad range of source parameters. These codes reduce the computation time by several orders of magnitude compared with the exact GS algorithm and therefore are an appropriate tool for the 3D forward modeling of the MHD wave.

In this paper, for the first time we examine the microwave emission modulation by the sausage mode building a 3D model with the numerical integration of the radiation transfer equation. To describe adequately variations of thermodynamic quantities in the sausage mode, we use an MHD approach similar to Antolin & Van Doorsselaere (2013), where forward modeling of the sausage mode modulation in EUV lines was investigated. In this paper, we focus only on the observational signatures of the GS intensity modulation by the sausage mode targeted at imaging instruments.

In Section 2, we describe the MHD models and codes used for the GS emission calculation. In Section 3, the results of the calculations are shown and compared with the previous models. In Section 4, we summarize our findings and discuss differences from the previous results obtained without spatial resolution.

2. MODELS

2.1. MHD Models

We chose our MHD model to be similar to the base model described by Antolin & Van Doorsselaere (2013). We assume an over-dense cylinder aligned with the magnetic field embedded in a low-β coronal environment. The equilibrium MHD plasma parameters, such as density, magnetic field, and gas pressure, experience a jump at the cylinder boundary that is taken to be discontinuous. The equilibrium is determined by the total pressure balance condition:

$$P_i + B_i^2/8\pi = P_e + B_e^2/8\pi, \tag{1}$$

where internal (external) values are denoted with a subscript $i(e)$, P is the plasma pressure, and B is the magnetic field magnitude. The effects of gravity, field-line curvature, and twist are ignored in this study. The formalism for the determination of MHD modes of this structure and for the derivation of their dispersion relations was developed by Zaitsev & Stepanov (1975) and Edwin & Roberts (1983).

The variation of the thermodynamic quantities is found by linearizing the perturbed ideal MHD equations about the magneto-static equilibrium (see Antolin & Van Doorsselaere 2013). For the sinusoidal perturbation leading to a standing mode, a divergence of the perturbed velocity will be $\nabla \cdot \mathbf{v} = -\Re(r)A\cos(\omega t)\sin(kz)$ in a cylindrical coordinate system (r, ϕ, z). Here $\mathbf{v} = (v_r, v_\phi, v_z)$ is the perturbed velocity, A is the total amplitude of the perturbation, ω is the angular frequency, and $k = \pi n/L$ is the longitudinal wavenumber with the longitudinal mode number n and the length of the cylinder L. The radial dependence of the divergence of velocity, $\Re$, in the case of a sausage mode must satisfy

$$\frac{d^2\Re}{dr} + \frac{1}{r}\frac{d\Re}{dr} - \kappa^2\Re = 0. \tag{2}$$

Here $\kappa^2 = (k^2C_{s,i/e}^2 - \omega^2)(k^2V_{A,i/e}^2 - \omega^2)/(C_{s,i/e}^2 + V_{A,i/e}^2)(k^2C_{t,i/e}^2 - \omega^2)$, $V_{A,i/e}$ is the Alfvén speed, and $C_{s,i/e}$ is the sound speed with the mass density $\rho_{i/e}$ and gas pressure $P_{i/e}$. $B_{i/e}$ is the unperturbed magnetic field strength, $C_{t,i/e}^2 = C_{s,i/e}^2V_{A,i/e}^2/(C_{s,i/e}^2 + V_{A,i/e}^2)$ is the squared tube speed, and $\gamma = 5/3$ is the ratio of specific heats.

The perturbed value of the magnetic field vector, $\mathbf{b} = (b_r, b_\phi, b_z)$, responsible for the modulation of the radio emission, can be found using the dispersion relation, and in a cylindrical coordinate system we have

$$b_r = \frac{\left(1 - \frac{k^2C_{t,i/e}^2}{\omega^2}\right)\left(C_{s,i/e}^2 + V_{A,i/e}^2\right)}{\omega^2 - k^2V_{A,i/e}^2}\frac{AB_{i/e}k}{\omega}\frac{d\Re}{dr}\sin(\omega t)\cos(kz) \tag{3}$$

$$b_\phi = 0 \tag{4}$$

$$b_z = \left(1 - \frac{k^2C_{s,i/e}^2}{\omega^2}\right)\frac{AB_{i/e}}{\omega}\Re(r)\sin(\omega t)\sin(kz). \tag{5}$$

Furthermore, perturbations of the direction of the magnetic field vector cause a variation of an angle θ between the LOS and $\mathbf{B}$ (B-LOS angle), which leads to an additional modulation of the GS emission. The B-LOS angle is determined in Cartesian coordinates:

$$\theta = \arccos\frac{\mathbf{B}\cdot\mathbf{L}}{|B||L|}, \tag{6}$$

where $\mathbf{L} = (\cos\theta_{\rm LOS}, 0, \sin\theta_{\rm LOS})$ is a unit vector determining the direction of the LOS in the XZ-plane with the $\theta_{\rm LOS}$, angle between the LOS and the main cylinder axis (or viewing angle), and $\mathbf{B} = (B_r\sin\phi, B_r\cos\phi, B_z)$. $\theta_{\rm LOS} = 90^\circ$ when the LOS is perpendicular to the main axis of the cylinder. The model cylinder and the aforementioned angles are shown schematically in Figure 1.

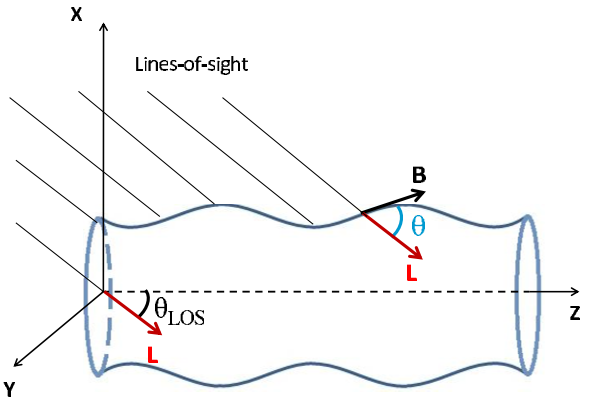

Figure 1. Sketch of the model cylinder with the sausage oscillations showing the B-LOS angle θ and the viewing angle $\theta_{\rm LOS}$ located in the same plane.
(A color version of this figure is available in the online journal.)

The number density N and temperature T of the thermal plasma will also exhibit perturbations in time and space:

$$N = \frac{A\gamma N_{i/e}\Re}{\omega}\sin(\omega t)\sin(kz), \quad (7)$$

$$T = \frac{A(\gamma-1)T_{i/e}\Re}{\omega}\sin(\omega t)\sin(kz), \quad (8)$$

where $N_{i/e}$ and $T_{i/e}$ correspond to the unperturbed quantities. The unperturbed thermodynamic quantities are linked through the ideal gas law for a fully ionized hydrogen gas $P_{i/e} = 2k_B N_{i/e} T_{i/e}$, where k_B is the Boltzmann constant.

The model by Antolin & Van Doorsselaere (2013) was originally adopted for the examination of the EUV line intensity modulation; therefore, non-flaring plasma parameters were used. For our model calculation we use typical parameters of flaring coronal plasma.

"Base" model. In the equilibrium state, we take the magnetic field strength inside the cylinder, $B_i = 50$ G, the internal thermal number density, $N_{Pi} = 10^{10}$ cm^{-3}, and external, $N_{Pe} = 3 \times 10^9$ cm^{-3}. Supposing the temperature inside the flare loop to be $T_i = 10$ MK and outside $T_e = 2$ MK, we get the magnetic field outside the loop, $B_e = 56$ G from the total pressure balance condition (Equation (1)). Correspondingly, the Alfvén speeds inside and outside the loop are estimated as $V_{Ai} = 1.09 \times 10^3$ km s^{-1} and $V_{Ae} = 2.2 \times 10^3$ km s^{-1}, respectively. The sound speed in the loop is $C_{Si} = 525$ km s^{-1}. The plasma β inside the cylinder is 0.28 and outside 0.01, compatible with the values found by Van Doorsselaere et al. (2011).

The normalized longitudinal wavenumber is $kR_0 = 2.24$, where $R_0 = 1$ Mm denotes the radius of the cylinder. This results in a longitudinal wave length $\lambda = 2\pi/k = 2.8$ Mm. The cylinder length $L = 8.4$ Mm. The phase speed of the sausage mode corresponding to the wavenumber k in the base model is $C_p = 1.8 \times 10^3$ km s^{-1}, and the period $P = 1.5$ s.

It is well known that if a dense plasma is present in a radio source, Razin suppression becomes important and can considerably decrease the GS emission and absorption coefficients at frequencies $f \leqslant f_R$ (Razin 1960a, 1960b). Here f_R is the Razin frequency defined as

$$f_R = 2f_p^2/3f_{B_\perp}, \text{where} f_{B_\perp} = f_B \times \sin\theta, \quad (9)$$

where f_p and f_B are the plasma frequency and gyrofrequency, respectively. So it is proportional to the ratio of the plasma number density to the component of the magnetic field strength perpendicular to the LOS: $f_R \approx 20N_p/B_\perp$. A high ambient density N_P and/or low magnetic field strength $B_\perp$ act to raise f_R.

In our base model, the Razin frequency varies from 4 GHz to 8 GHz, when the viewing angle changes from 85° to 30°, respectively. Therefore, the low-frequency part of the GS spectrum will be affected by Razin suppression. Previous studies have found (see Section 1) that, depending on the presence or absence of the Razin effect, the low-frequency ($f < f_{\rm peak}$) GS emission can show in-phase or anti-phase behavior compared to the high-frequency ($f > f_{\rm peak}$) emission due to the sausage oscillations. To investigate the latter case, when the Razin suppression does not influence the low-frequency part of the spectrum, we consider the model with a low density.

"Low-density" model. We take the internal thermal number density, $N_{Pi} = 4 \times 10^9$ cm^{-3}, and external, $N_{Pe} = 10^9$ cm^{-3}, in the equilibrium state. To preserve the total pressure balance condition, the magnetic field strength was taken to be $B_i = 160$ G inside the cylinder and $B_e = 161$ G outside it. The other parameters are similar to the base model. Correspondingly, the Alfvén speeds inside and outside the loop are calculated as $V_{Ai} = 5.5 \times 10^3$ km s^{-1} and $V_{Ae} = 1.1 \times 10^4$ km s^{-1}, respectively. The sound speed in the loop $C_{Si} = 524$ km s^{-1}, the phase speed $C_p = 7.7 \times 10^3$ km s^{-1}, and the period of the sausage mode $P = 0.35$ s. The plasma β inside the cylinder is 0.01. The Razin frequency varies from 0.5 GHz to 1 GHz for the view angle 85°–30°; hence, the Razin suppression is negligible in the frequency range of interest (1–100 GHz).

In both models, the cylinder is filled with nonthermal mildly relativistic electrons, perturbation of which is similar to thermal plasma density given by Equation (7).

Numerically, our model consists of a $204 \times 204 \times N_z$ grid. N_z denotes the number of points in the z-direction and is chosen to keep the same spatial resolution in x, y, and z axes, about 25 km, for all different LOS angles when calculating the GS emission. A higher resolution model, four times greater, was also investigated to assess convergence of the numerical procedure. The temporal resolution is taken as 30 time steps per period.

Figure 2 shows a snapshot of our base model, representing a cut along the middle axis of the cylinder. The snapshot is taken at a time of one-fourth of the period P under view angle 90°. The cylinder is located between $x = -1$ Mm and $x = 1$ Mm. The total magnetic field strength is obtained as $B = \sqrt{B_r^2 + B_z^2}$. The sausage mode creates in-phase perturbations between the magnetic field, density, and temperature and anti-phase perturbations between the density and the cylinder cross section. The antinodes of the field magnitude, density, temperature, and radius oscillation (one of them is indicated by a cross) coincide with the nodes of the B-LOS angle perturbation. Antinodes of the angle variation are located closer to the cylinder surface, similar to the nodal structure of the radial velocity.

At the location of an antinode, the magnetic field and density oscillate about 6% (4%) around mean values in the base model (low-density model). The maximum variation of B-LOS angle is 2° (1°.1) in the base model (low-density model). The maximum perturbation of the loop radius is very small, 25 km, that is, 2.5% of the radius of the loop.

2.2. GS Emission Calculation

The microwave radiation from solar flares is usually produced by mildly relativistic particles gyrating in a magnetic field, by the GS mechanism. During the decay phase of flares, the

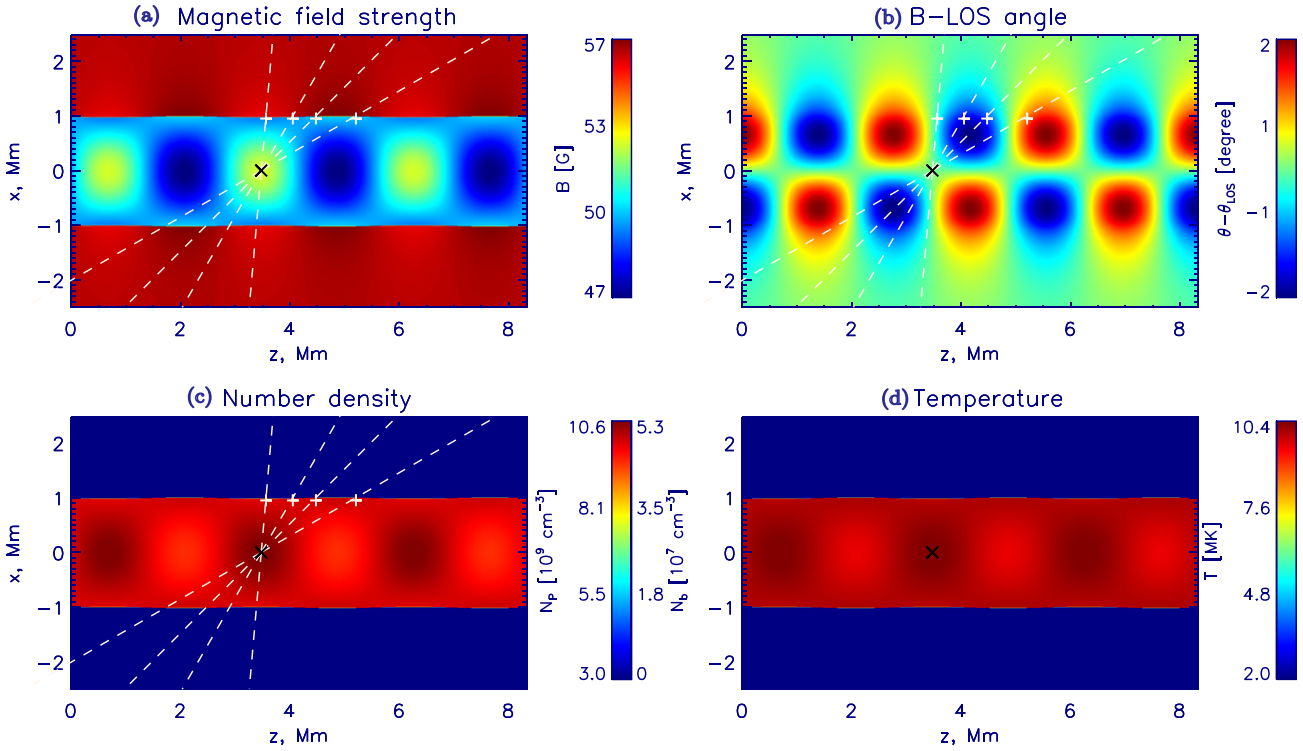

Figure 2. Structure of the (a) magnetic field strength, (b) perturbation of the B-LOS angle, (c) thermal and nonthermal number density, and (d) temperature perturbations along a cross section through the center of the cylinder. Snapshots are taken at $t = 1/4P$ under viewing angle 90°. The cross indicates an antinode of the field magnitude, density, and temperature oscillation. The LOSs passing through the antinode at different viewing angles, 85°, 60°, 45°, and 30°, are shown by dashed lines, and their intersections with the surface of the cylinder by plus signs.

(A color version of this figure is available in the online journal.)

bremsstrahlung mechanism, that is, free–free emission and absorption, can play an additional role.

The exact formulae for the GS emissivities and absorption coefficients (Eidman 1958) are cumbersome and extremely slow computationally. Therefore, a number of simplified approximations have been developed (for a review see Fleishman & Kuznetsov 2010). The most widely used analytical approximation of Dulk & Marsh (1982) derived for a limited range of harmonic numbers (20–100) and moderate viewing angles relative to the magnetic field (30°–80°) has an accuracy within tens of percent. The thermal plasma effects are not included. Due to the limited range of parameters, it is difficult to take into account emission propagation effects.

The most suitable for our modeling are the modern fast GS codes developed by Fleishman & Kuznetsov (2010). These codes include the contribution of the free–free emission and are applicable for a broad range of isotropic and anisotropic distributions and plasma parameter combinations. In the most recent version, the numerical integration of the radiative transfer equation in an inhomogeneous medium is implemented, and a possible change of the polarization in the areas of the transverse magnetic field is taken into account (Kuznetsov et al. 2011). As a result of the calculation using the code with radiative transfer, arrays of the left- and right-polarized emission intensities, I_f^L and I_f^R, are obtained for the selected frequencies f under the assumption that the emission source is observed from the distance of one astronomical unit (e.g., it is located at the Sun and observed from the Earth).

A significant advantage of these codes is that they can be optimized for accuracy or computation speed with a full range of intermediate options. Depending on these options, the computation error remains within 1%–10%, while the computation time is reduced by an order of magnitude compared with the exact formulae. For our computations we selected the fastest "continuous" code, which yields continuous spectra (i.e., without the discrete low-frequency harmonic structure) but provides appropriate accuracy. Even using the fastest code requires about one day of a standard PC CPU for our model.

2.3. Nonthermal Electron Distributions

To describe the nonthermal electron distributions, we used analytical functions $G(E, \mu)$ built into the GS codes of Fleishman & Kuznetsov (2010), which are written in the factorized form:

$$G(E, \mu) = u(E)g(\mu), \tag{10}$$

that is, a product of the energy distribution function $u(E)$ and the angular distribution function $g(\mu)$. Here $\mu = \cos\alpha$, where α is the electron pitch angle (i.e., the angle between the electron momentum and the magnetic field vector).

We selected two different electron distributions over kinetic energy $E = mc^2(\gamma - 1)$. The first is a single power-law distribution:

$$u(E) = aE^{-\delta}, \quad \text{for } E_{\min} < E < E_{\max}, \tag{11}$$

where the electron spectral index $\delta = 3.5$, $E_{\min} = 0.1$ MeV, and $E_{\max} = 10$ MeV. The normalization constant a equals

$$a = \frac{N_{bi/e}}{2\pi} \frac{\delta - 1}{E_{\min}^{1-\delta} - E_{\max}^{1-\delta}}, \tag{12}$$

with the number density inside the loop $N_{bi} = N_{Pi}/200$ and outside the loop $N_{be} = 0$. Since the density of energetic electrons is more than two orders of magnitude lower than the

density of thermal plasma, it does not violate the total pressure balance condition.

Another distribution has a double power-law spectrum over energy and takes into account low-energetic electrons, from 0.01 MeV, often detected in solar flares via hard X-ray data. It is described by the following expression:

$$u(E)dE = dE \begin{cases} a_1 E^{-\delta_1}, & \text{for } E_{\min} < E \leqslant E_{\rm break}, \\ a_2 E^{-\delta_2}, & \text{for } E_{\rm break} \leqslant E < E_{\max}, \end{cases} \quad (13)$$

where the electron spectral indices for the low-energy part $\delta_1 = 1.5$, and for the high-energy part $\delta_2 = 3$, $E_{\min} = 0.01$ MeV, $E_{\max} = 10$ MeV, and $E_{\rm break} = 0.5$ MeV. To make the function continuous in the above expression, $a_1 E_{\rm break}^{-\delta_1} = a_2 E_{\rm break}^{-\delta_2}$. The normalization factor is given by

$$a_1^{-1} = \frac{2\pi}{N_{b,i/e}} \left(\frac{E_{\min}^{1-\delta_1} - E_{\rm break}^{1-\delta_1}}{\delta_1 - 1} + E_{\rm break}^{\delta_2-\delta_1} \frac{E_{\rm break}^{1-\delta_2} - E_{\max}^{1-\delta_2}}{\delta_2 - 1} \right), \quad (14)$$

where $N_{bi} = N_{Pi}/4000$ is the nonthermal number density at $E \geqslant E_{\rm break}$ and $N_{be} = 0$. This gives N_{bi} one order of magnitude less than the thermal density at $E \geqslant 0.01$ MeV.

The distribution over pitch angle is isotropic: $g(\mu) = \text{const} = (1/2)$. Although there is evidence of different kinds of anisotropy in many cases, comparison of the modulation amplitude for the isotropic and the loss-cone distributions showed that the difference is not sufficient to allow distinction between the two cases (Mossessian & Fleishman 2012).

We assume the formation of a steady-state distribution of the nonthermal electrons in the case of the absence of MHD oscillations in the loop. Since our goal is to investigate the impact of MHD oscillations on the GS emission of the flare loop, all other dynamics, such as electron energy losses due to Coulomb collisions or radiation, are not considered at this stage.

3. CALCULATION RESULTS

In order to obtain the observational signatures of the sausage mode suitable for imaging instruments, the total intensity has been calculated at 4 viewing angles relative to the cylinder axis, 85°, 60°, 45°, and 30°, and at 12 frequencies between 1 GHz and 100 GHz.

The total intensity as a function of the observed frequency, f, is determined as

$$I_f = I_f^L + I_f^R. \quad (15)$$

Further, we integrate the intensity over pixels of sizes 0.″5 and 2.″8 imitating different angular resolution of radioheliographs, such as ALMA and CSRH. The latter pixel size is also equal to the diameter of the model loop. Since our findings for two different nonthermal energy distribution functions do not show qualitative differences, we will mostly present the results of calculations obtained with the single power-law spectrum, unless otherwise specified.

3.1. Spacial Structure of the Intensity

Figure 3 shows the intensity, I_f, obtained by integrating the radiation along the LOS at viewing angles 85° (left column) and 60° (right column) for the base model. The intensity is shown at three frequencies 2.5 GHz (top), 5 GHz (middle), and 100 GHz (bottom) representing the three characteristic cases: low frequency ($f < f_{\rm peak}$), a peak frequency, $f_{\rm peak}$, and high frequency ($f > f_{\rm peak}$) emission, accordingly. Since the nonthermal number density outside the loop $N_{be} = 0$, this area is not shown. The snapshot is taken at one-quarter of the period, coinciding with that of Figure 2. The increase of radio brightness corresponds to the areas of stronger magnetic field strength and higher density at all three frequencies. The centers of radio brightness coincide with the antinode location denoted by crosses.

In Figure 4, the intensity is shown for viewing angles 45° and 30°. The middle panels represent intensity at 6 GHz and 8 GHz where the peak frequency is located for the 45° and 30° cases, respectively. The brightness variation along the cylinder is strongly suppressed in the case of 45°. Interestingly, for the 30° viewing angle, the antinode locations coincide with the brightness minimum at all three frequencies. The same is true for 2.5 GHz in the 45° case. This is because the spatial variation of the B-LOS angle becomes more significant for the small viewing angles. For instance, it reaches 4.5% for $\theta_{\rm los} = 45°$. As a result, the centers of radio brightness are shifted from the antinode location.

Figures 5 and 6 show the integrated intensity for the low-density model. The spectral peak for this model is located between 7 and 10 GHz. Intensity at these frequencies is represented in the middle panels. The apparent diameter of the radiating tube is the widest at 2.5 GHz since the opacity is higher at lower frequencies. The variation of radio brightness along the cylinder is much smaller at this frequency, meaning that the loop is optically thick ($\tau \gg 1$). The antinode location at 2.5 GHz is shifted from the brightness maximum and minimum.

3.2. Temporal Variation of the Intensity

The whole intensity spectra at three moments of time, $P/4$, $P/2$, and $3P/4$, of the mode period P are shown in Figure 7. The intensity is integrated over a pixel of size 0.″5 with the center located on the LOS crossing an antinode of the cylinder rotated at different angles to the observer.

An increase of the intensity is clearly seen for both models during the first half of the period (dashed line) when the magnetic field and nonthermal number density increase in the center of the cylinder at a specific antinode location. Conversely, in the second half of the period (dash-dotted line) the intensity falls. The exception is the 30° case, where completely opposite behavior of the spectrum is observed in the base model. Spectral variation is qualitatively similar for different energy spectra of the nonthermal electrons, single power-law (top row) and double power-law (middle row). In the latter case, the resulting intensity is much smaller due to the lower density of high-energy electrons at $E = 0.1$ MeV: $N_b = 3 \times 10^7$ cm^{-3} compared with 2×10^8 cm^{-3} in the single power-law distributions.

Variations of spectra in the low-density model are significantly less. Note the opposite trend of the peak frequency shift with the view angle: $f_{\rm peak}$ increases with the decrease of the LOS angle $\theta_{\rm LOS}$ in case of the base model (from 5 to 8.5 GHz), whereas it drops down in the case of the low-density model (from 10 to 7 GHz). The reason is the strong suppression of the GS emission in the base model due to the Razin effect at frequencies $f \leqslant f_R$, where f_R changes from 4 GHz for view angle 85° to 8 GHz for 30°. For the double power-law electron distribution this quantity is about 10% higher due to the equivalent increase in the total density of electrons (thermal and nonthermal). Consequently, corresponding intensity spectral maxima are slightly shifted to the right as compared with the single power-law case in the base model. In the case of the

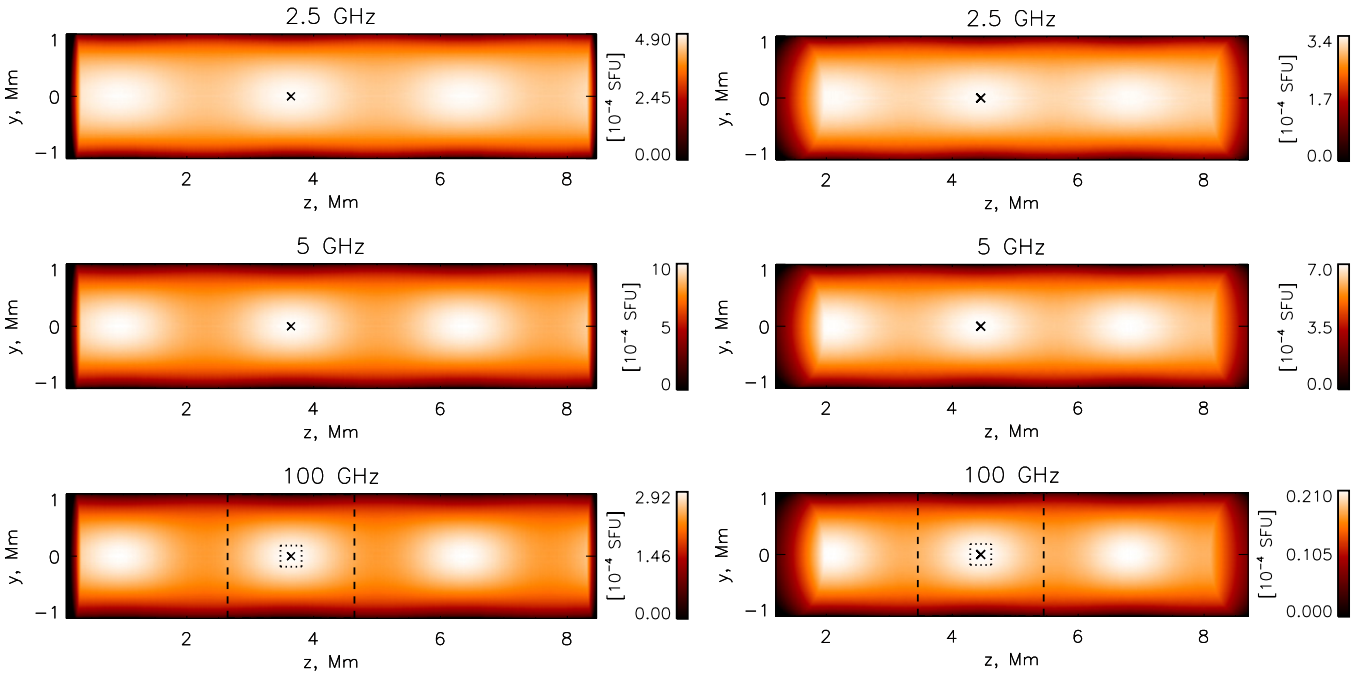

Figure 3. Intensity obtained by integrating the radiation along the LOS at angles of (left column) 85° and (right column) 60° at frequencies 2.5 GHz, 5 GHz, and 100 GHz. Snapshots are taken at $t = P/4$ for the base model. Crosses denote the location of an antinode, and pixels of sizes 0.″5 (dotted line) and 2.″8 (dashed line) are shown in the bottom panels.

(A color version of this figure is available in the online journal.)

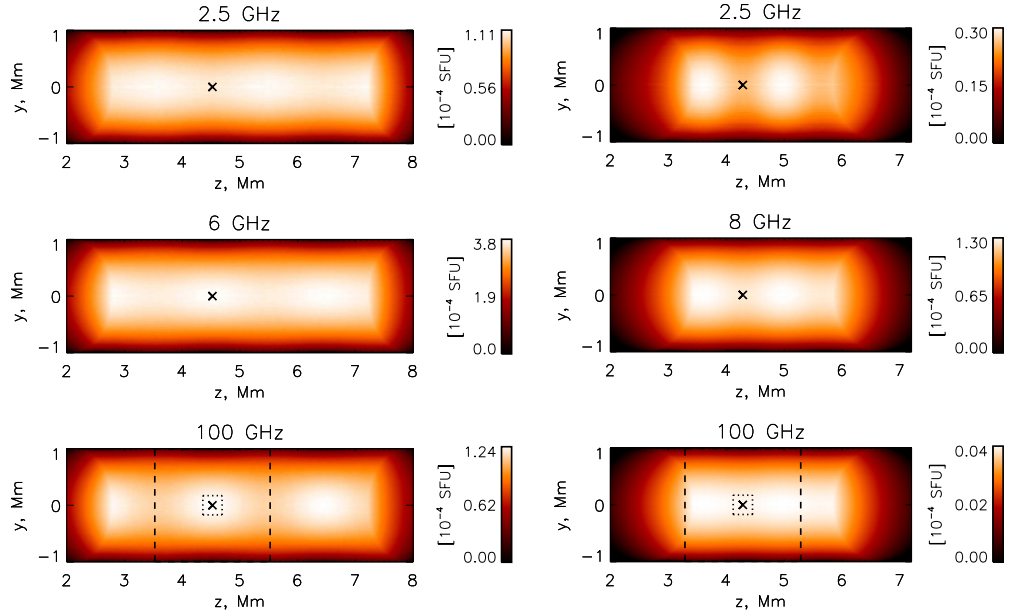

Figure 4. Same as Figure 3, but for the viewing angles 45° (left) and 30° (right) and middle panel for the frequencies 6 GHz (left) and 8 GHz (right).

(A color version of this figure is available in the online journal.)

low-density model, the double power-law electron distribution shifts the spectral maxima to the left, to 5.5 GHz for 85° and 4.5 GHz for 30° angles because of the decrease in the optical depth.

In the case of a spatial resolution of 2.″8, approximately equal to the tube's diameter $2R$ (or 0.7λ), variations of spectra are negligible and not shown here.

Figure 8 (top and middle rows) represents relative intensity variations, $\delta I/I_0$, on the LOS crossing the antinode at viewing angles (from left to right) 85°, 60°, 45°, and 30° in the base model. This quantity is calculated as $\delta I/I_0 = (I_f(t) - I_{f0})/I_{f0}$, where $I_f(t)$ is the time series of the intensity at the selected frequency f, and I_{f0} is the corresponding equilibrium value. Therefore, this quantity represents a modulation depth of intensity. Perturbations of the magnetic field, densities, and the B-LOS angle averaged along the LOS inside the cylinder are shown in the bottom panels by solid, dotted, and dash-dotted curves, accordingly.

The oscillation of emission observing at angles 85° and 60° with the spatial resolution 0.″5 at all frequencies is found to be in-phase with the averaged variation of the magnetic field strength and density. However, when looking at 45°, the emission at 2.5 GHz oscillates in anti-phase to B and N; for 30° angle this is true for all frequencies. In the case of the double power-law

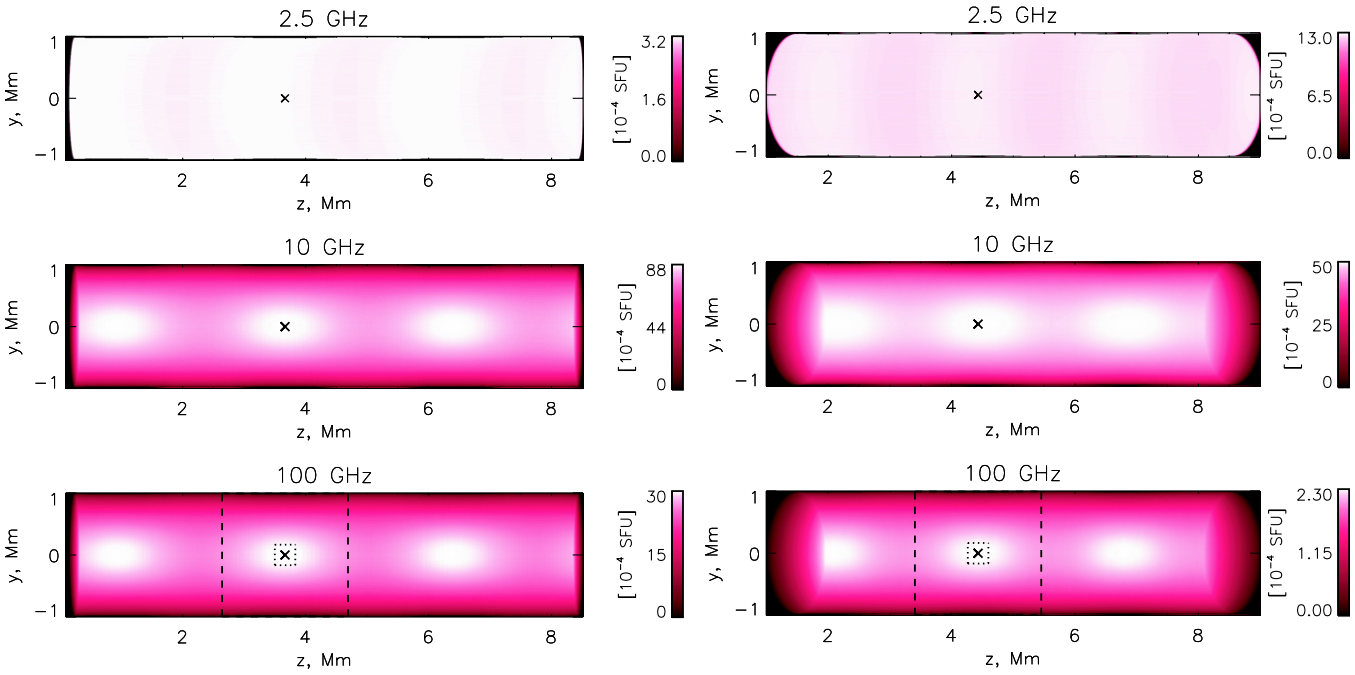

Figure 5. Same as in Figure 3, but for the low-density model and middle panels for 10 GHz.
(A color version of this figure is available in the online journal.)

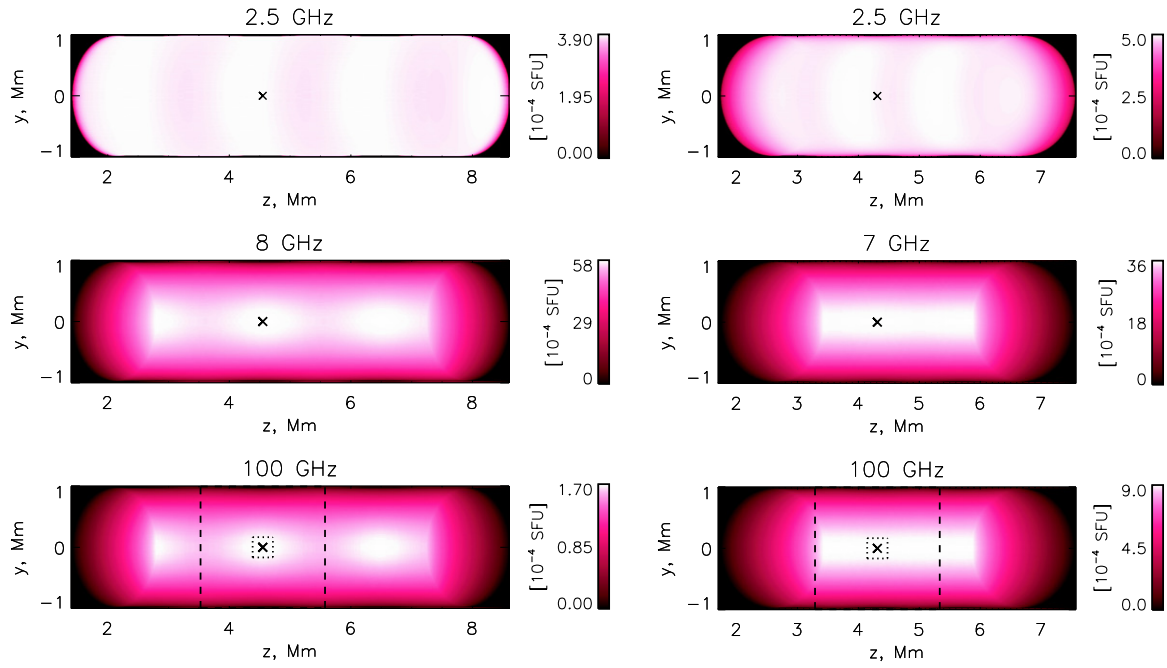

Figure 6. Same as in Figure 4, but for the low-density model and middle panels for the frequencies 8 GHz (left) and 7 GHz (right).
(A color version of this figure is available in the online journal.)

distribution of the nonthermal electrons, the phase relations are the same as found with the single power-law spectra and not shown here.

Our findings for the 85° and 60° are consistent with the previously obtained results (e.g., Reznikova et al. 2007; Mossessian & Fleishman 2012), which predicted in-phase variation of intensity at high ($f > f_{\rm peak}$) and low ($f < f_{\rm peak}$) frequencies in the case of strong Razin suppression. The reason is that the Razin effect makes the low-frequency emission optically thin. The optical depth of the cylinder is shown in Figure 9 by the solid line for the base model. Although the peak frequency $f_{\rm peak}$ is in the range of 5–8.5 GHz, the optical depth τ at all studied frequencies is indeed less than unity. It is even smaller when using the double power-law spectrum of the nonthermal electrons. At the same time an anti-phase emission variation at viewing angle 30° and partially at 45° is not in agreement with previous studies.

Improving the spacial resolution from 0.″5 to the best possible in our model, 0.″03, increases the modulation amplitude maximum by a factor of 1.05, but does not change the picture qualitatively (not shown here). Therefore, a spatial resolution better than $\lambda/8$, which equals 0.″5 in our model, is not

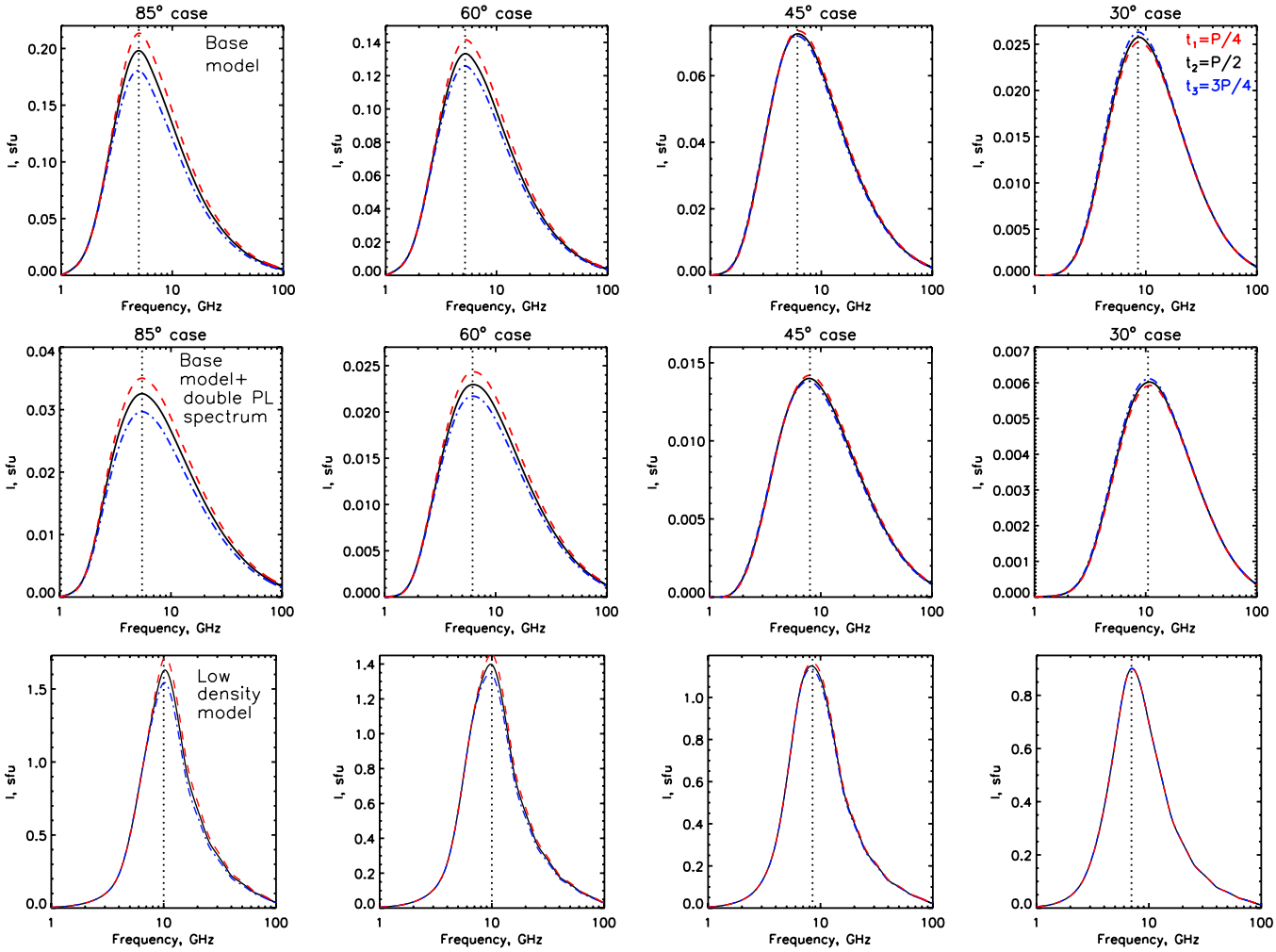

Figure 7. Intensity spectra integrated over a pixel of 0.″5 centered at an antinode of the cylinder rotated at an angle of (from left to right) 85°, 60°, 45°, and 30° to an observer at times $P/4$ (dashed), $P/2$ (solid), and $3P/4$ (dash-dotted) of the mode period P. The top and middle rows are for the base model, and the bottom row is for the low-density model. The middle row corresponds to the model with the double power-law spectrum of the nonthermal electrons. The peak frequency is marked by the dotted line.

(A color version of this figure is available in the online journal.)

necessary. However, reducing the resolution to 2.″8 (or 0.7λ) decreases the modulation depth by more than a factor of four. For the 30° case the phase was even inverted since the pixel of 2.″8 includes two nodes located on both sides of the selected antinode.

Relative intensity variations in the low-density model are shown in Figure 10. Similar to the base model, in the case of the spatial resolution 0.″5, the oscillation of emission at viewing angle 30° is in anti-phase to the emission at all other viewing angles and to the magnetic field perturbation averaged along the LOS. Moreover, observations at each particular viewing angle would give in-phase oscillations of radio signals between all three frequencies.

Again, the latter result contradicts the findings of the previous simulations by Kopylova et al. (2002), Reznikova et al. (2007), and Mossessian & Fleishman (2012), who predicted an anti-phase variation of the intensity at optically thick ($f < f_{\rm peak}$) and optically thin ($f > f_{\rm peak}$) frequencies when the Razin effect is unimportant (low-density model). Indeed, in the low-density model, the peak frequency $f_{\rm peak}$ is in the range of 7–10 GHz for 30°–85° views, respectively. The optical depth crosses unity at the corresponding frequencies (Figure 9, dashed line). Therefore, one would expect to have an anti-phase variation of intensity between low (2.5 and 5 GHz) and high (100 GHz) frequencies. However, our model simulations do not show such a behavior.

The first reason for such a contradiction is that previous models did not take into account the inhomogeneity of the emitting source along the LOS, assuming that the magnetic field and density oscillate in phase within the entire source. Second, the variation of the B-LOS angle was not taken into account at all.

Let us show it quantitatively comparing our results with the famous approximations made by Dulk & Marsh (1982) for the case of an isotropic electron distribution in pitch angle and with a power law in energy. According to their empirical expressions, the dependence of the GS intensity on the magnetic field strength, B, nonthermal electron number density, N_b, and B-LOS angle, θ, is

$$I_f \propto N_b B^{2.93} (\sin\theta)^{1.85}, \quad \text{if } \tau \ll 1 \tag{16}$$

and

$$I_f \propto B^{-0.8} (\sin\theta)^{-0.57}, \quad \text{if } \tau \gg 1. \tag{17}$$

We have taken into account the electron spectral index $\delta = 3.5$ used in our models.

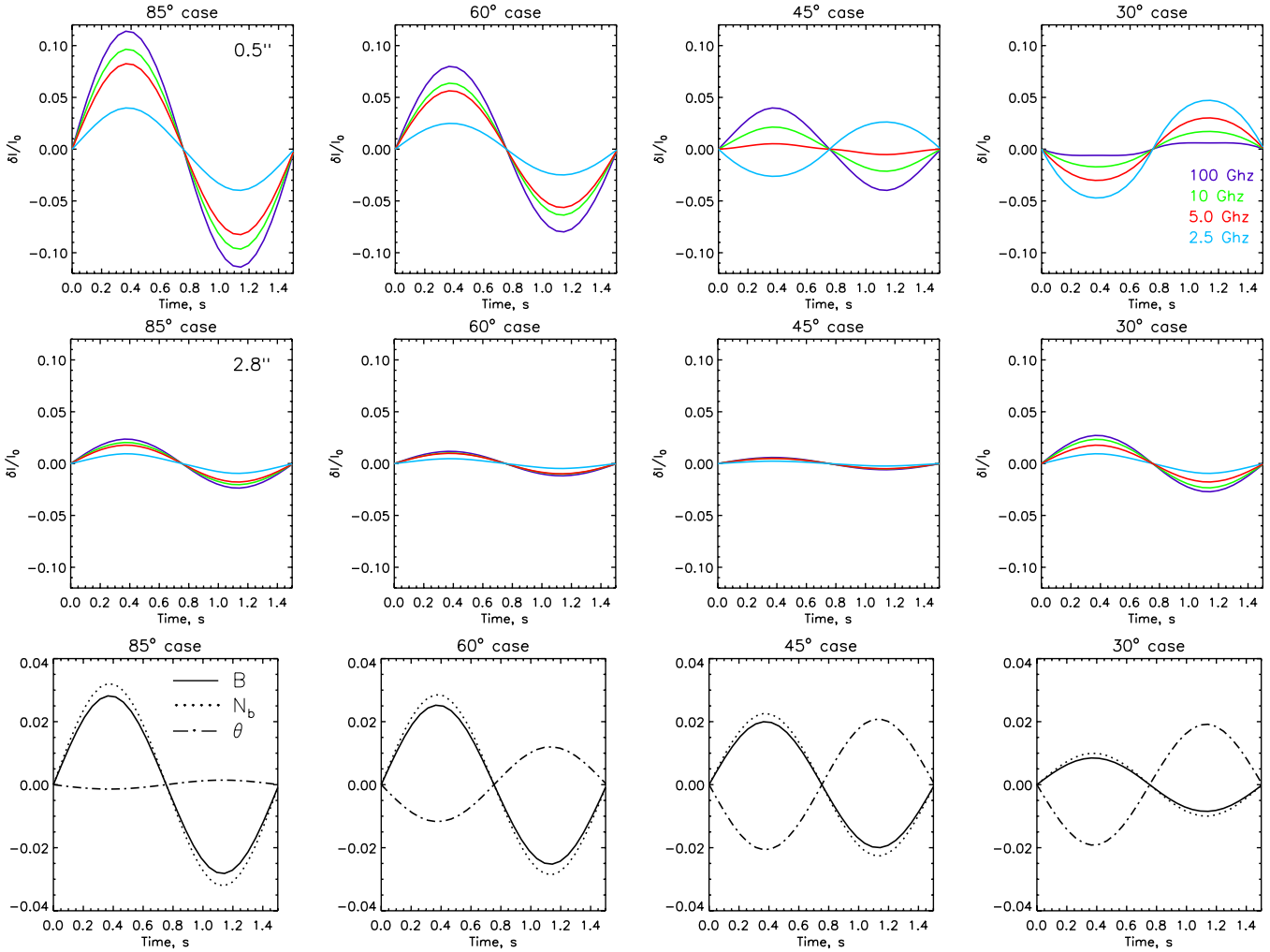

Figure 8. Temporal variation of the normalized intensity integrated over pixel sizes 0.″5 (top row) and 2.″8 (middle row) in the base model for the four viewing angle cases. The color coding of different frequencies is denoted in the top-right plot. Bottom row: temporal variation of the initial parameters averaged along the LOS. The relative perturbations of the magnetic field, density, and B-LOS angle are shown by solid, dotted, and dash-dotted curves, respectively.

(A color version of this figure is available in the online journal.)

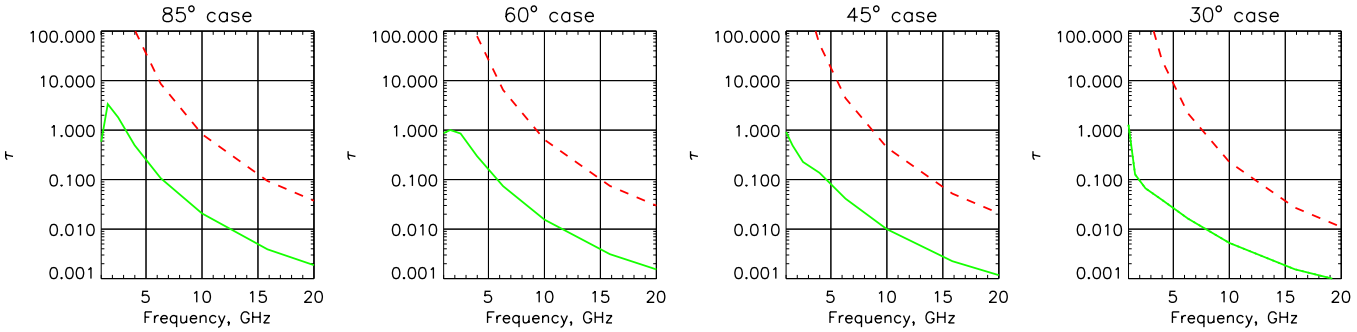

Figure 9. Optical depth of the emitting source for the base model (solid curve) and for the low-density model (dashed curve).

(A color version of this figure is available in the online journal.)

Expression 16 shows that in the optically thin regime, the intensity variations must occur in phase with B, N_b, and angle θ perturbations. In the case of the quasi-perpendicular emission propagation (85°), expression 16 gives variations of the intensity $\delta I/I = 12\%$ (8%) under the average along the LOS perturbations of the magnetic field $\delta B/B = 2.8\%$ (2%) and nonthermal density $\delta N/N = 3.3\%$ (2%) in the base model (low-density model). Note that in the quasi-perpendicular case, perturbations of the angle θ are negligibly small (0.15%). Similarly, estimates give variations of the intensity 9% (6%) for 60° viewing angle, 5% (4%) for 45° viewing angle, and −0.07% (−0.02%) for 30° viewing angle. We have taken into account an anti-phase with magnetic field and density perturbations of the angle θ, which strongly decreases the modulation depth of the microwave emission at angles of 60° and 45° and even inverts the phase at the angle 30°. These estimates are in a good agreement with the simulated modulation depth of emission at 100 GHz, at which the cylinder is optically thin in both models.

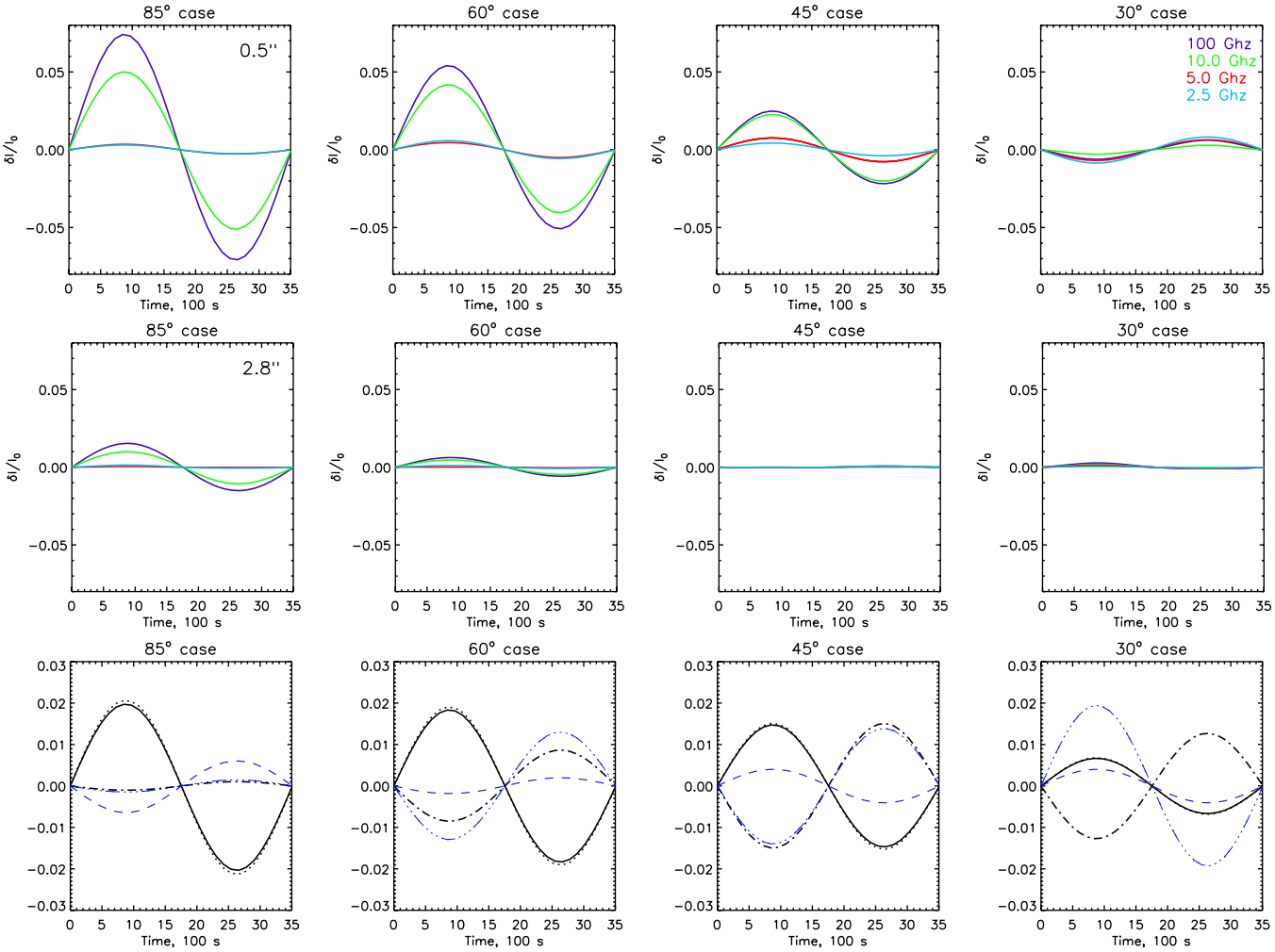

Figure 10. Same as Figure 8, but for the low-density model. Dashed and dash-dot-dot lines indicate relative perturbations of the magnetic field and B-LOS angle, respectively, near the cylinder surface in the point of intersection with the LOS.

(A color version of this figure is available in the online journal.)

According to expression (17), the variation of the optically thick emission (at $f < 7$ GHz in the low-density model) must occur in anti-phase with the field B and angle θ variations and must be several times weaker than in the optically thin regime. Indeed, the modulation of the intensity at 2.5 GHz and 5 GHz is considerably smaller than at 100 GHz.

We have to emphasize that in the optically thick regime the emission comes from the area close to the cylinder surface, and, therefore, variation of the plasma parameters in the cylinder center does not influence the intensity at $f < f_{\rm peak}$. Our 3D MHD model of the loop with the sausage wave shows that the perturbation of the initial parameters across the loop is inhomogeneous: depending on the viewing angle, they may occur in phase or in anti-phase near to the surface of the cylinder compared to the center. The perturbations of the magnetic field and the B-LOS angle near the cylinder surface in the point of the LOS intersection are shown in Figure 8 (bottom) by dashed and dash-dotted curves, accordingly. The use of these parameters for the estimate with the expression (17) gives a modulation depth $\delta I/I = 0.5\%$ for the 85° case, 0.6% for the 60° case, 0.4% for the 45° case, and -1.2% for the 30° case. Our results again agree with these estimates.

The modulation of the low-frequency emission in the base model cannot be compared with Dulk & Marsh (1982) approximations since they do not take into account Razin suppression. Under conditions of strong Razin suppression ($f \leqslant f_R$) the sensitivity of GS emission to the magnetic field strength variations is considerably enhanced. That is well seen from the expression, obtained in the relativistic approach for the intensity of the synchrotron emission (Gundyrev & Razin 1995):

$$I_f \propto \left(\frac{2f}{3f_R}\right)^{1-\delta} \exp\left(-\frac{3^{2/3} f_R}{2f}\right). \quad (18)$$

The intensity variations are in phase with the magnetic field strength variations: the weaker the magnetic field, the lower the intensity. Note, however, that in the case of the sausage mode we have oscillations of the magnetic field, density, and viewing angle. So, the above simple consideration does not work and the modulation depth at low frequencies is expected to be weaker.

The obtained results may be applied to any sausage mode wavenumber. Thus, in the global mode, the magnetic field perturbation has a maximum at the loop apex, and the nodes coincide with the loop footpoints. Hence, results presented for the antinode and node locations are applicable to the loop top and footpoints, respectively.

4. CONCLUSION

The modulation of the GS emission by fast sausage MHD oscillations was modeled for typical flaring parameters. For the first time a 3D model was adapted for this purpose. In addition, we have taken into account the variation of the angle between the magnetic field vector and the LOS. It was never done before when modeling the sausage mode.

Two models were investigated: the base model with the Razin suppression at low frequencies ($f < f_{\rm peak}$), and the low-density model in which the Razin effect was unimportant at all examined frequencies (1–100 GHz). Also, two different distributions of the nonthermal electrons over energy were considered: a single power law with $E_{\rm min} = 0.1$ MeV and a double power law with $E_{\rm min} = 0.01$ MeV.

The temporal intensity variation was analyzed on the LOS crossing the antinode with different spatial resolution and under different viewing angles. As a result, we have found that emission at three frequencies, $f < f_{\rm peak}$, $f = f_{\rm peak}$, and $f > f_{\rm peak}$, oscillates in phase in the low-density model. The same is true for the base model with the exception of the 45° viewing angle case. The phase relations remain the same, independently of the nonthermal electron distribution over energy (single or double power law). This finding contradicts previous predictions made with simpler models lacking a spatial resolution.

Such a contradiction occurs for the following reasons. As we mentioned before, previous models did not include the B-LOS angle variations, which are in anti-phase with the magnetic field and density variations and therefore strongly decrease the modulation depth of the microwave emission when observing at 60° and 45°, and even invert the phase in the 30° case. This is the first reason. Second, previous models assumed that the magnetic field and density oscillate in phase within the entire source. Our 3D MHD model shows that the sausage wave creates inhomogeneous perturbations of the initial parameters across the loop: depending on the viewing angle, they may occur in phase or in anti-phase near the surface of the cylinder compared to its center. Such strong LOS geometrical dependence on the ensuing intensity has recently been reported in Antolin & Van Doorsselaere (2013) for the case of EUV intensity modulation from sausage modes. Moreover, the decrease of the spatial resolution from 0.″5 to 2.″8 resulted in the inverted phase in the case of 30° viewing angle.

Consequently, a phase difference of π between the oscillation optically thin and optically thick regime in the case of the negligible Razin suppression cannot serve as an observational signature of the sausage mode, as well as an in-phase behavior of low- and high-frequency radiation in the case of strong Razin suppression. The overall picture is more complicated, where phase relations strongly depend not only on the plasma parameters in the flare region, but also on the viewing angle and the spatial resolution of the particular radio heliograph.

We acknowledge funding from the Odysseus Programme of the FWO Vlaanderen and from the EUs 7th Framework Programme as an ERG with grant number 276808. The research carried out by V.E.R. is partly supported by grant MC FP7-PEOPLE-2011-IRSES-295272. This research is in the frame of the Belspo IAP P7/08 CHARM network. V.E.R. is grateful to Dr. A. Kuznetsov and Dr. G. Fleishman for very helpful comments on the use of their code and to Dr. V. Melnikov for the discussions of the results.

REFERENCES

Antolin, P., & Van Doorsselaere, T. 2013, A&A, 555, A74
Aschwanden, M. J. 1987, SoPh, 111, 113
Dulk, G. A., & Marsh, K. A. 1982, ApJ, 259, 350
Edwin, P. M., & Roberts, B. 1983, SoPh, 88, 179
Eidman, V. Y. 1958, JETP, 7, 91
Fleishman, G. D., & Kuznetsov, A. A. 2010, ApJ, 721, 1127
Gundyrev, A. G., & Razin, V. A. 1995, A&AT, 6, 229
Inglis, A. R., Nakariakov, V. M., & Melnikov, V. F. 2008, A&A, 487, 1147
Kopylova, Y. G., Stepanov, A. V., & Tsap, Y. T. 2002, AstL, 28, 783
Kupriyanova, E. G., Melnikov, V. F., Nakariakov, V. M., & Shibasaki, K. 2010, SoPh, 267, 329
Kuznetsov, A. A., Nita, G. M., & Fleishman, G. D. 2011, ApJ, 742, 87
Lin, R. P., Dennis, B. R., Hurford, G. J., et al. 2002, SoPh, 210, 3
McLean, D. J., Sheridan, K. V., Stewart, R. T., & Wild, J. P. 1971, Natur, 234, 140
Melnikov, V. F., Reznikova, V. E., Shibasaki, K., & Nakariakov, V. M. 2005, A&A, 439, 727
Mossessian, G., & Fleishman, G. D. 2012, ApJ, 748, 140
Nakajima, H., Nishio, M., Enome, S., et al. 1994, IEEEP, 82, 705
Nakariakov, V. M., & Melnikov, V. F. 2009, SSRv, 149, 119
Nakariakov, V. M., Melnikov, V. F., & Reznikova, V. E. 2003, A&A, 412, L7
Nakariakov, V. M., & Verwichte, E. 2005, LRSP, 2, 3
Razin, V. A. 1960a, IzVUZ, 3, 584
Razin, V. A. 1960b, IzVUZ, 3, 921
Reznikova, V. E., Melnikov, V. F., Su, Y., & Huang, G. 2007, ARep, 51, 588
Rosenberg, H. 1970, A&A, 9, 159
Van Doorsselaere, T., De Groof, A., Zender, J., Berghmans, D., & Goossens, M. 2011, ApJ, 740, 90
Vasheghani Farahani, S., Hornsey, C., Van Doorsselaere, T., & Goossens, M. 2014, ApJ, 781, 92
Zaitsev, V. V., & Stepanov, A. V. 1975, Geomagn. Aeron. Fiz. Soln., 37, 3
Zaitsev, V. V., & Stepanov, A. V. 1982, SvAL, 8, 132
Zaitsev, V. V., Stepanov, A. V., Urpo, S., & Pohjolainen, S. 1998, A&A, 337, 887
Zimovets, I. V., & Struminsky, A. B. 2010, SoPh, 263, 163